

Supporting Information to Multiband Plasmonic Sierpinski Carpet Fractal Antennas

Francesco De Nicola,^{1,*} Nikhil Santh Puthiya Purayil,^{1,2} Davide Spirito,³
Mario Miscuglio,^{3,4} Francesco Tantussi,⁵ Andrea Tomadin,¹ Francesco
De Angelis,⁵ Marco Polini,¹ Roman Krahne,³ and Vittorio Pellegrini¹

¹*Graphene Labs, Istituto Italiano di Tecnologia,
Via Morego 30, 16163 Genova, Italy*

²*Physics Department, Università degli studi di Genova,
Via Dodecaneso 33, 16146 Genova, Italy*

³*Nanochemistry Department, Istituto Italiano di Tecnologia,
Via Morego 30, 16163 Genova, Italy*

⁴*Chemistry and Industrial Chemistry Department,
Università degli studi di Genova, Via Dodecaneso 33, 16146 Genova, Italy*

⁵*Plasmon Nanotechnologies, Istituto Italiano di Tecnologia,
Via Morego 30, 16163 Genova, Italy*

1. GENERATION OF THE SIERPINSKI CARPETS

A Lindenmayer system (L-system)¹ is a deterministic approach to iteratively generate complex fractal objects starting from a finite alphabet of symbols and a collection of production rules. These rules are simple prescriptions, such as inflations, that expand each symbol into larger strings of symbols starting from an initial axiom, which is considered the seed of the recursive construction. L-systems provide a computationally efficient and general method to produce many fractal shapes. In Figure S1, a L-system implementation for the generation of the first five order of complexity of a Sierpinski carpet (SC) is depicted. The initial axiom is F , while the rules to iterate are $(F \rightarrow F + F - F - F - UGD + F + F + F - F)$, $(G \rightarrow GGG)$. Both the variables F and G means “draw forward”, while $+/-$ stand respectively for “turn right/left by 90° ”, and U/D are respectively “pen up/down”.

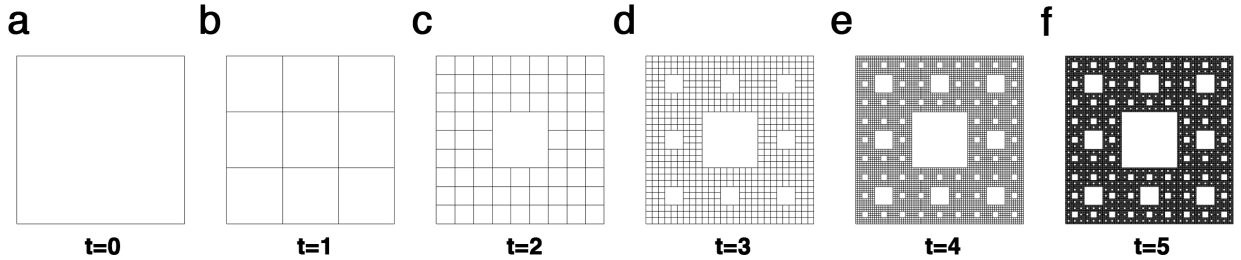


FIG. S1. **a-f**, L-system algorithm for the SC generation at different fractal orders $t = 0-5$.

2. EXPERIMENTAL SIERPINSKI CARPETS

The main properties of the experimental SCs shown in Figure S2 are summarized as follows. The size of the sub-cells at a fractal order t is $L_t = L_0 3^{-t}$, where $L_0 = 10 \mu\text{m}$ is the size of the initial cell. At each iteration the side of the sub-cells is reduced by a factor $\mathcal{L} = 3$. Since the number of empty sub-cells in the SC increases by a factor $\mathcal{N} = 8$ at every iteration, the fractal dimension is $d_H = \log \mathcal{N} / \log \mathcal{L} \approx 1.89$. The total area of the fractal is $\mathcal{A}_t = \sum_t N_t A_t$, with $N_t = 8^{t-1}$ and $A_t = L_t^2$ the number and area of the square elements, respectively, while the fractal spatial filling fraction is $f = \mathcal{A}_t / L_0^2$. In Table S1, the experimental main quantities associated to the five orders of the Au SC are reported.

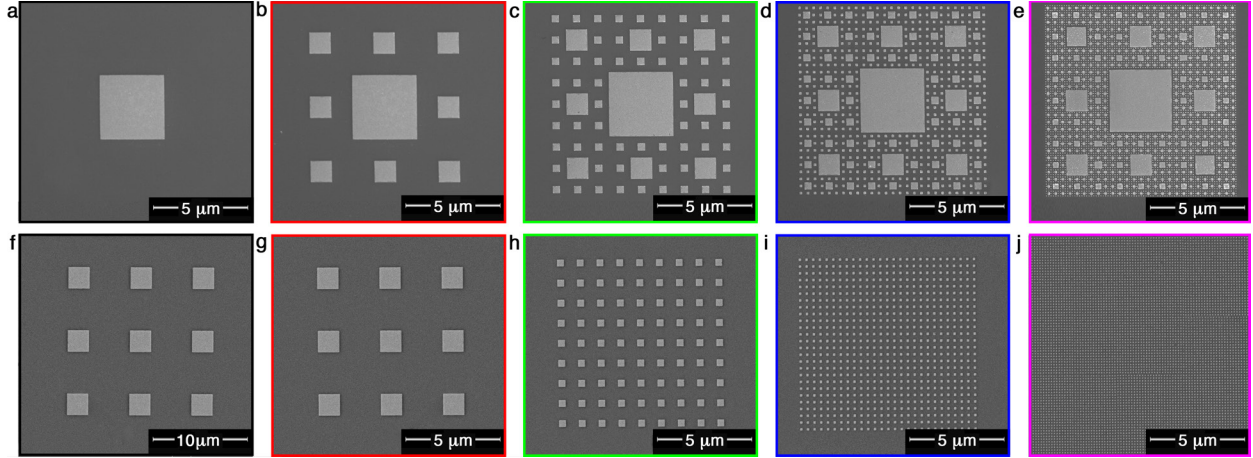


FIG. S2. **a-e**, Color-coded SEM micrographs of 35 ± 3 nm thick Au SCs deposited on a Si/SiO₂ substrate for fractal orders $t = 1$ (black), $t = 2$ (red), $t = 3$ (green), $t = 4$ (blue), $t = 5$ (magenta). **f-j**, Micrographs of 35 ± 3 nm thick Au periodic arrays with square size L_1 (black), L_2 (red), L_3 (green), L_4 (blue), L_5 (magenta), as a comparison.

t	\mathcal{N}_t	N_t	L_t (μm)	A_t (μm^2)	\mathcal{A}_t (μm^2)	f
1	8	1	3.382 ± 0.050	11.438 ± 0.338	11.438 ± 0.338	0.114 ± 0.003
2	64	8	1.121 ± 0.011	1.257 ± 0.025	21.494 ± 0.200	0.214 ± 0.002
3	512	64	0.390 ± 0.017	0.152 ± 0.013	31.222 ± 0.832	0.312 ± 0.008
4	4096	512	0.130 ± 0.007	0.017 ± 0.002	39.926 ± 1.024	0.399 ± 0.010
5	32768	4096	0.044 ± 0.003	0.002 ± 0.001	48.118 ± 4.096	0.481 ± 0.041

TABLE S1. Summary of the Au SC experimental main quantities.

3. FRACTAL ANALYSIS OF THE CARPET RECIPROCAL LATTICE

We employed the box-counting algorithm² (Gwyddion) to determine the fractal dimension of a SC reciprocal lattice for fractal order $t = 5$, as shown in Figure S3. The algorithm works as follows. A square array with periodicity x is superimposed on the reciprocal lattice image. Initially x is set at $\varepsilon/2$ (where ε is the size of the image), resulting in an array of 2^2 boxes. Then $N(x)$ is the number of all the squares containing at least one pixel of the image. The array periodicity x is then reduced stepwise by factor of 2 and the process is repeated until

x equals to the distance between two adjacent pixels. The slope of the $\log N(x)$ - $\log 1/x$ plot gives a fractal dimension $d_H = 1.91 \pm 0.02$.

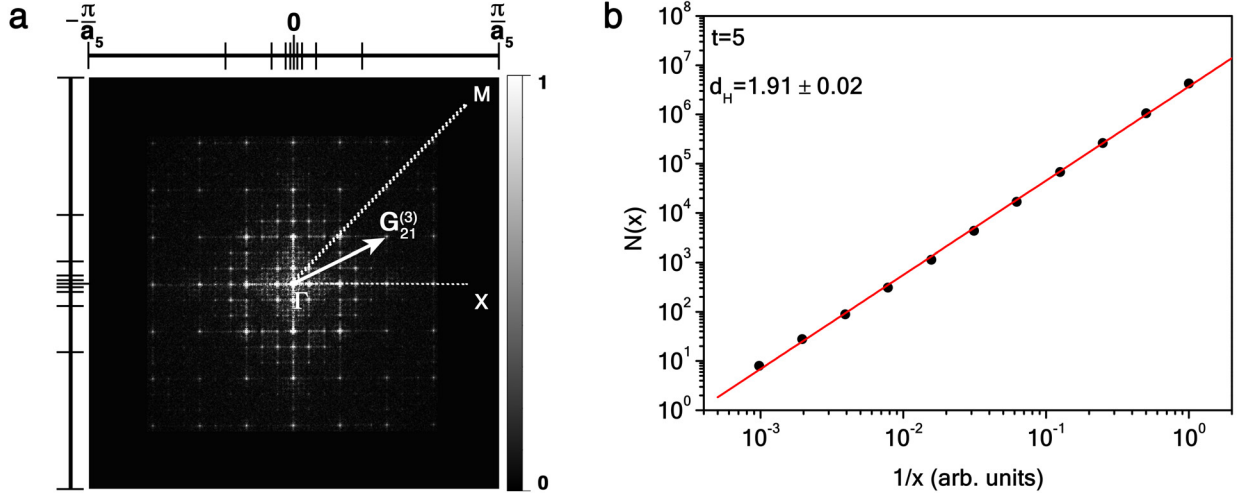


FIG. S3. **a**, Reciprocal lattice of the SC at $t = 5$ calculated by fast Fourier transform of its SEM micrograph. The $\Delta = \overline{\Gamma X}$ and $\Sigma = \overline{\Gamma M}$ direction in the fractal reciprocal lattice are marked along with the first pseudo-Brillouin zones $[-\pi/a_t, \pi/a_t]^2$ for the different orders. **b**, Box-counting algorithm applied on the SC reciprocal lattice. The fit returns a fractal dimension $d_H = 1.91 \pm 0.02$.

4. POLARIZATION-INDEPENDENT AU SIERPINSKI CARPETS

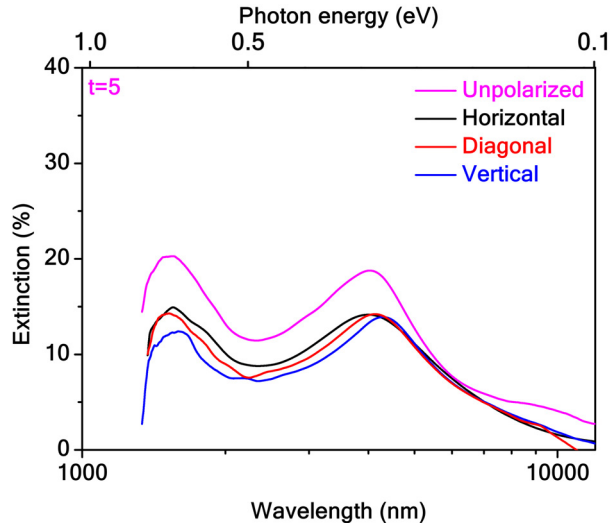


FIG. S4. Experimental extinction spectra of SCs at $t = 5$ for unpolarized light (magenta solid curve) and horizontal (black solid curve), diagonal (red solid curve), and vertical (blue solid curve) polarization.

5. FANO RESONANCES OF DIFFRACTION-MEDIATED PLASMONS

Generally, the microscopic origin of the Fano resonance arises from the constructive and destructive interference of a narrow discrete resonance with a broad spectral line or continuum³. The interference of the incident and re-emitted light generates a complex near-field pattern and may give rise to either strong enhancement (constructive interference) or strong suppression (destructive interference) of the electromagnetic field. The first observation of this asymmetric lineshape in optics is related to the Wood anomaly⁴. This phenomenon can be explained by the interaction between the diffracted orders of a grating coupler and the plasmon resonances, as a result of radiative coupling. Also, Fano resonances may occur when Mie dipolar modes mix with higher-order modes.

In figure S5, we fitted the extinction resonances in a 45 nm thick SC for $t = 5$ with the Fano total scattering cross-section³

$$\sigma = \frac{\left(\frac{q\Gamma}{2} + \omega - \omega_0\right)^2}{\left(\frac{\Gamma}{2}\right)^2 + (\omega - \omega_0)^2}, \quad (1)$$

with Γ the resonance width, ω_0 the resonance center, and q the Fano parameter, which measures the ratio of the scattering amplitudes related to the two different modes. The fit returns $q_1 = 0.9 \pm 0.2$ (dipole), $q_2 = 1.3 \pm 0.2$ (dipole), $q_3 = 3.5 \pm 0.1$ (quadrupole), and $q_4 = 7.9 \pm 0.4$ (octapole) Fano parameters.

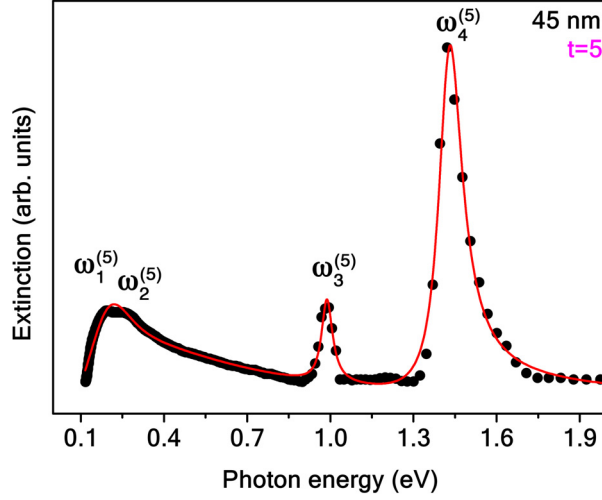


FIG. S5. Experimental extinction spectrum of a 45 nm thick SC for $t = 5$. Fit of the $\omega_1^{(5)}$, $\omega_2^{(5)}$, $\omega_3^{(5)}$, and $\omega_4^{(5)}$ resonances with the Fano function (red solid curve).

6. SCALING OF DIFFRACTION-MEDIATED PLASMONS

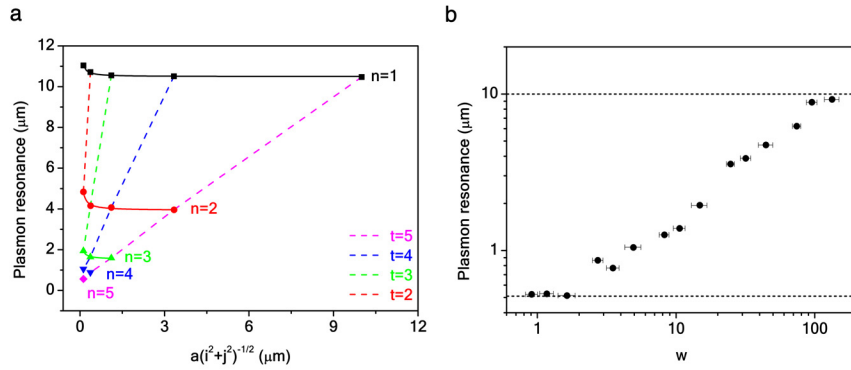


FIG. S6. **a**, Scaling relation between the experimental LSP resonance $\lambda_n^{(t)}$ and the lattice parameter a_t . **b**, Experimental wavelength of LSP resonance as a function of $w_t = L_t/h$. At short wavelengths plasmons are cut off by Au interband transitions, while at long wavelengths they are damped by radiative diffracted orders.

7. ELECTROMAGNETIC SIMULATION OF THE AU SIERPINSKI CARPETS

We used CST Microwave Studio software for finite elements method simulations in order to evaluate the electromagnetic near-field distributions of the Au SCs, and highlight the differences between the fractal orders and their related periodic square lattices. For our study we considered Au SCs deposited on CaF₂ substrates. The complex dielectric constant of the Au squares constituting the fractals was described by Rakic et al.⁵, while the dielectric constant of the CaF₂ substrate was given by Malitson⁶. The design of our structures is illustrated in the inset of Figure S7. A linearly polarized plane wave (TM) radiation source with a varying wavelength is placed above the structure at normal incidence. A perfectly matched layer bounding box was implemented. The boundary conditions of the system were considered as periodic. We used a sufficiently fine mesh that gave steady and mesh-independent results for the near-field distributions. A direct solver was chosen for the solution method (MUMPS), which allowed cluster computing for parallelization.

In the main text, we discussed the electric near-field distribution on Au SCs. Here, analogous conclusions can be drawn for the magnetic near-field distribution, as shown for orders $t = 1-4$ in Figure S7. Under quasi-static conditions ($\lambda \gg L$), the dipolar magnetic near-field of the central element is remarkably affected by the dipoles of the neighboring elements smaller in size, corresponding to the successive orders of the SC. Therefore, the near-field couples with elements of different size, redistributing the local scattered radiation on the overall structure, thus hierarchically localizing the magnetic near-field on the self-similar structures⁷. In this way, an efficient transfer of LSP excitations towards progressively smaller length scales occurs in the SC, as its order of complexity increases.

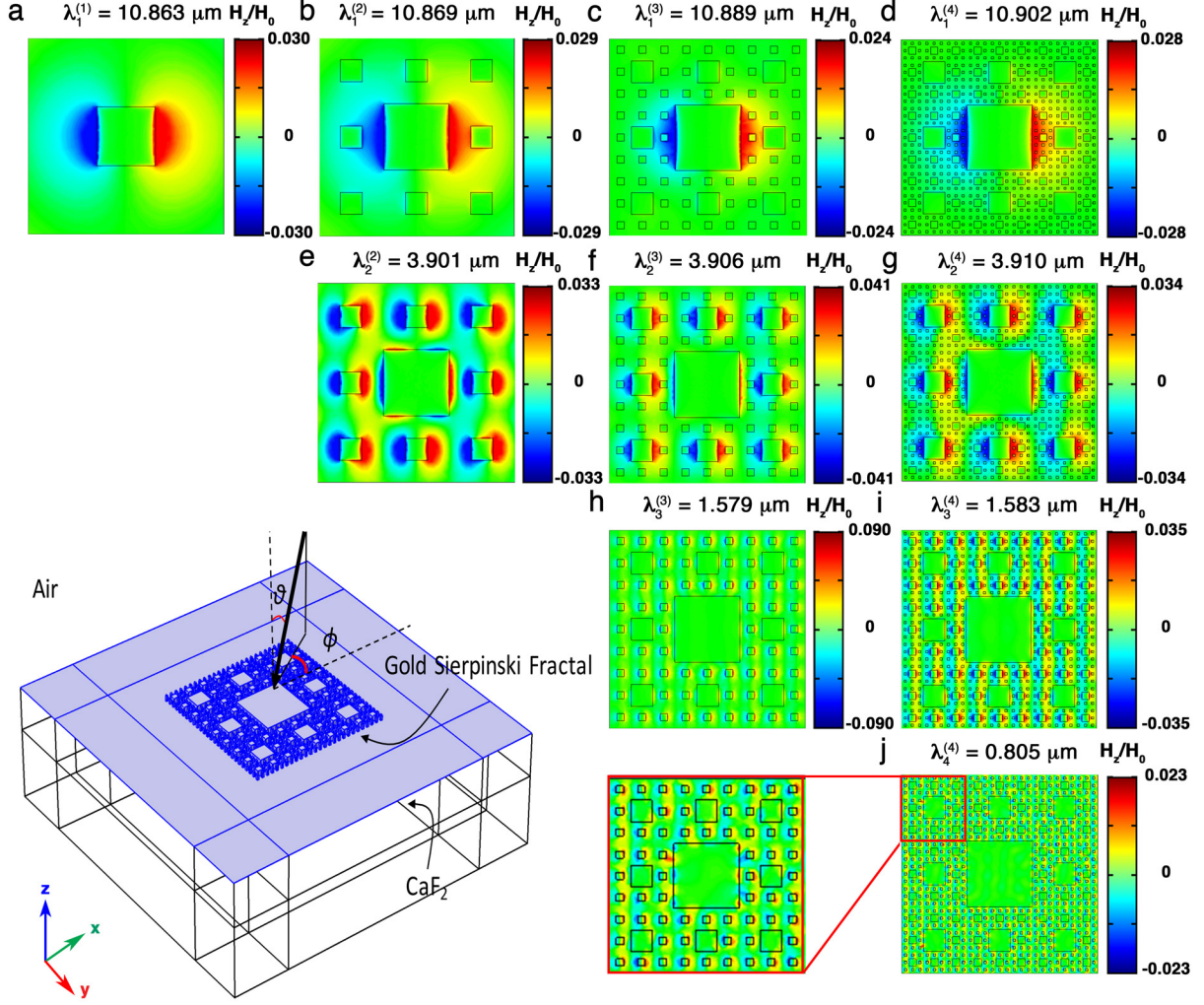


FIG. S7. Finite element method simulations of plasmonic Au SCs. Simulated magnetic near-field enhancement (H_z/H_0) distribution of SCs for orders $t = 1-4$ (from left to right) at their resonances $\lambda_1^{(t)}$ (**a-d**), $\lambda_2^{(t)}$ (**e-g**), $\lambda_3^{(t)}$ (**h-i**), $\lambda_4^{(t)}$ (**j**). The incident wave points in the $\theta = 0$ direction orthogonal to the plane of incidence with the magnetic field in the $\phi = 0$ direction. The phase is set to zero in order to maximize the field intensity. Inset, a sketch of the modeled Au SC deposited on a CaF₂ substrate.

8. SURFACE ENHANCED RAMAN SPECTROSCOPY

8.1. Enhancement factor

The SERS enhancement factor was calculated for orders $t = 1-5$ of the SC by the relation

$$EF_{sers} = \frac{\langle I_{sample} \rangle}{\langle I_{Au} \rangle} \frac{A_{Au}}{A_{sample} N_{sample}}, \quad (2)$$

where $\langle I_{sample} \rangle$ is the average Raman intensity in adu units (1 adu = 1 count/mWs) at $\omega^* = 1655 \text{ cm}^{-1}$ measured over the SC maps, $A_{Au} = 0.785 \text{ } \mu\text{m}^2$ is the area of the laser beam spot on the reference Au film, $A_{sample} = L_t^2$ is the area of the smallest square of the fractal at order t for which the Raman enhancement is maximum, N_{sample} is the number of the smallest squares within the beam spot area (Figure S8), and $\langle I_{Au} \rangle$ is the average Raman intensity in adu units at ω^* measured over the map of the ideally smooth reference Au film. Notably, electromagnetic simulations showed that the reference Au film surface roughness ($\approx 3 \text{ nm}$) provides itself an electric field enhancement factor of about 2, therefore a Raman intensity factor $\langle I_{ref} \rangle / \langle I_{Au} \rangle \approx 16$ with respect to an ideally smooth Au surface. It is worth noting that all the experimental conditions for the sample and the reference are exactly the same.

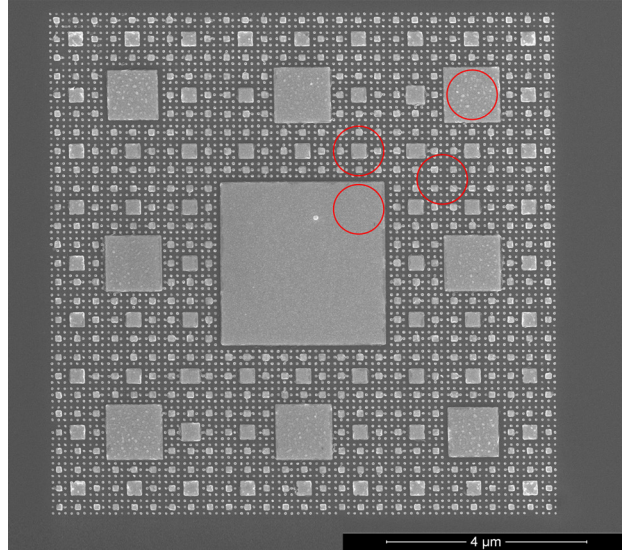


FIG. S8. Scanning electron microscopy micrograph of a SC for $t = 5$. Red solid circles mark the size of the Raman laser beam spots in order to estimate the number N_{sample} of the smallest structures that contribute to the maximum SERS enhancement factor. For $t = 1-5$, $N_{sample} = 1, 1, 4, 30$.

8.2. Mapping

The experimental enhanced electric field E_z/E_0 distribution of a SC for $t = 5$ order obtained from SERS mapping the BCB vibrational mode ω^* at $\lambda_{ex} = 633$ nm, together with its cross section along the marked solid red line are reported in Figure S9a. The cross section in Figure S9b clearly shows a field enhancement of a factor about 10 between the region on the central square of size L_1 and the adjacent region with squares of size L_4 and L_5 .

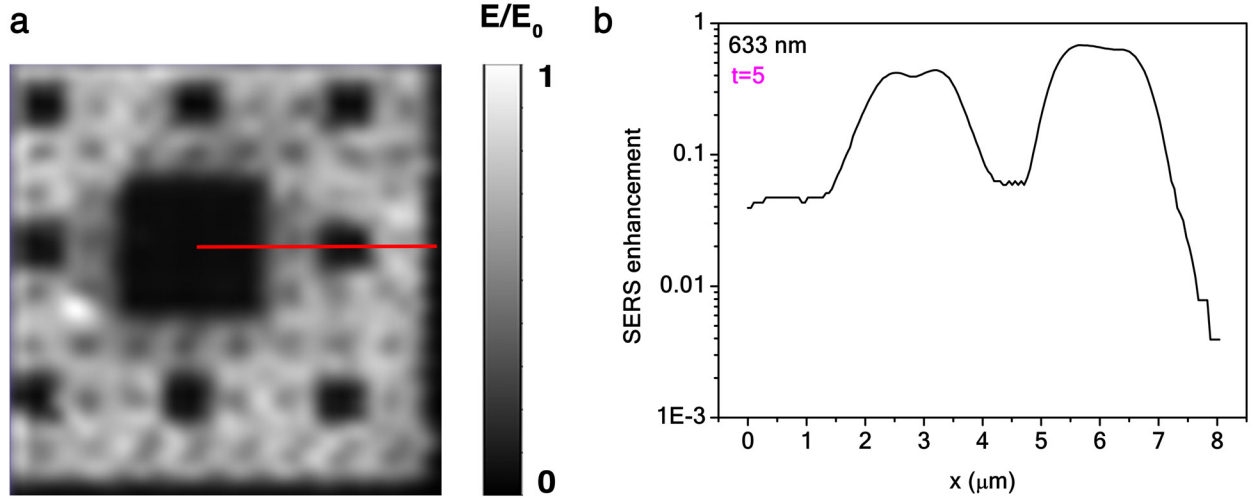


FIG. S9. **a**, Experimental electric field enhancement E_z/E_0 distribution of a SC for fractal order $t = 5$. **b**, Cross section of the map along the marked solid red line.

* francesco.denicola@iit.it

¹ A. Lindenmayer and P. Prusinkiewicz, *The Algorithmic Beauty of Plants* (Springer, New York, 1990).

² C. Douketis, Z. Wang, T. L. Haslett, and M. Moskovits, Fractal Character of Cold-deposited Silver Films Determined by Low-Temperature Scanning Tunneling Microscopy, *Phys. Rev. B* **51**, 11022 (1995).

³ B. Luk'yanchuk, N. I. Zheludev, S. A. Maier, N. J. Halas, P. Nordlander, H. Giessen, and C. T. Chong, The Fano Resonance in Plasmonic Nanostructures and Metamaterials, *Nat. Mater.* **9**, 707 (2010).

- ⁴ A. Hessel and A. A. Oliner, A New Theory of Wood's Anomalies on Optical Gratings, *Appl. Opt.* **4**, 1275 (1965).
- ⁵ A. D. Rakić, A. B. Djurišić, J. M. Elazar, and M. L. Majewski, Optical Properties of Metallic Films for Vertical-Cavity Optoelectronic Devices, *Appl. Opt.* **37**, 5271 (1998).
- ⁶ I. H. Malitson, A Redetermination of Some Optical Properties of Calcium Fluoride, *Appl. Opt.* **2**, 1103 (1963).
- ⁷ S. V. Boriskina, A. Gopinath, and L. D. Negro, Optical Gap Formation and Localization Properties of Optical Modes in Deterministic Aperiodic Photonic Structures, *Opt. Express* **16**, 11813 (2008).